BIOCHEMISTRY
including biophysical chemistry & molecular biology
Article

Biochemistry **2010,** *49,* 8967–8977 8967
DOI: 10.1021/bi100953t

Mutations Alter the Geometry and Mechanical Properties of Alzheimer's Aβ(1−40) Amyloid Fibrils[†]

Raffaella Paparcone,[‡] Matthew A. Pires,[‡] and Markus J. Buehler*[,‡,§]

[‡]*Laboratory for Atomistic and Molecular Mechanics, Department of Civil and Environmental Engineering, Massachusetts Institute of Technology, 77 Massachusetts Avenue, Room 1-235A&B, Cambridge, Massachusetts 02139-4301, and* [§]*Center for Computational Engineering, Massachusetts Institute of Technology, 77 Massachusetts Avenue, Cambridge, Massachusetts 02139-4301*

Received June 14, 2010; Revised Manuscript Received August 3, 2010

ABSTRACT: The identification of more efficient therapies for defeating severe degenerative diseases like Alzheimer's is a major goal of drug discovery research. Realizing this ambitious goal will likely require a series of molecular insights that shed light on the fundamental mechanisms that drive the formation, growth, stability, and toxicity of Aβ(1−40) amyloid fibrils, one of the most abundant species found in affected brain tissues and potentially a major player in the progression of Alzheimer's disease. Amyloid fibrils feature a highly ordered and dense network of hydrogen bonds, a universal feature of all amyloid structures, which is realized by a highly regular stacking of small β-units that are each stabilized by an intrapeptide salt bridge. Here we report a series of molecular dynamics simulations of large-scale amyloid fibrils with local mutations that result in the disruption of the key intrapeptide salt bridge. We demonstrate that mutations, through alterations in the nature of the salt bridge, have a significant effect on the geometry and mechanical properties of the amyloid fibril. We specifically observe a severe decrease in amyloid fibril periodicity (the period length) of up to 43%, and extreme variations of the Young's modulus (a measure of the fibril's mechanical stiffness) of up to 154%. These results confirm that, while on one hand side chains are not involved in the formation of the β-strands composing the inner core of the amyloid structure, their presence, size, and interactions can be crucial in determining the larger-scale properties of amyloid fibrils. Our results imply that interactions mediated by side chains could be a potential target for novel approaches to drug design and the development of molecular therapies for amyloid disorders such as Alzheimer's disease, through the chemical deactivation of key functional groups that are responsible for promoting the growth of the fibrils, for promoting their chemical and mechanical stability, and for furthering their aggregation in amyloid plaques.

The socioeconomic impact of neurological disorders, and in particular Alzheimer's disease, is incredibly high, and growing as our population ages. In the United States alone, according to the Alzheimer's Association, there are more than 5.3 million patients and the total annual cost reaches $148 billion (*1*, *2*). In the last 20 years, experimental findings have suggested different explanations for the origin of these disorders. According to a common hypothesis, this fatal neurodegenerative disorder is caused by the aggregation and deposition of amyloid fibrils in brain tissues, and this phenomenon is involved in neuronal atrophy typically observed when the disease progresses (*3*). Amyloids are polypeptide molecules assembled into β-sheet-rich linear aggregates (*4*), and as reported by Eisenberg and collaborators, almost all complex proteins, even though not structurally similar, have short segments that if exposed to an appropriate environment (and sufficiently flexible) are capable of triggering amyloid formation (*5*).

Even though amyloids were originally primarily associated with the above mentioned neurodegenerative diseases, evidence of functional roles (*6*−*9*) in different natural contexts such as bacterial coatings, catalytic scaffolds, and epigenetic information transfers confirms that the amyloid configuration is accessible to a wide variety of proteins and may even be utilized as a physiological mechanism in some settings (*10*, *11*). Moreover, their highly ordered hierarchical structure makes amyloids a powerful tool for creating interesting nanostructured materials (*12*−*16*), given their exceptional sturdiness, elasticity, and strength as well as their remarkable stability under chemical, mechanical, and thermal stress (*10*, *17*, *18*). These issues explain the increasing interest in amyloid protein materials from various scientific communities (medical, materials science, biochemistry) to identify links between their structure and pathological and physiological properties.

Here we focus on the 2-fold symmetric Aβ(1−40) amyloid fibrils that are directly related to Alzheimer's disease (*6*). They are formed after sequential cleavage of the amyloid precursor protein (APP) that is expressed in many tissues and concentrated in the synapses of neurons. The Aβ(1−40) amyloid fibril structure has been identified through solid state nuclear magnetic resonance (ssNMR) data (*19*), where it was found that it consists of a single β-unit stabilized by a salt bridge (*20*−*22*) (Figure 1), and the overall fiber is composed of the repetition of those units along the fiber axis. The so-formed layers stack in register and display a specific (2- or 3-fold) symmetry with respect to the growth axis (*23*, *24*), as well as a characteristic twist angle that is homogeneously distributed along the fiber axis. The stability of the resulting fibrous structure is partly due to a dense and highly organized network of hydrogen bonds (here also abbreviated as

[†]This research was supported by Office of Naval Research Grant NN00014-08-1-0844.

*To whom correspondence should be addressed. E-mail: mbuehler@mit.edu. Phone: (617) 452-2750. Fax: (617) 324-4014.

Published on Web 08/23/2010

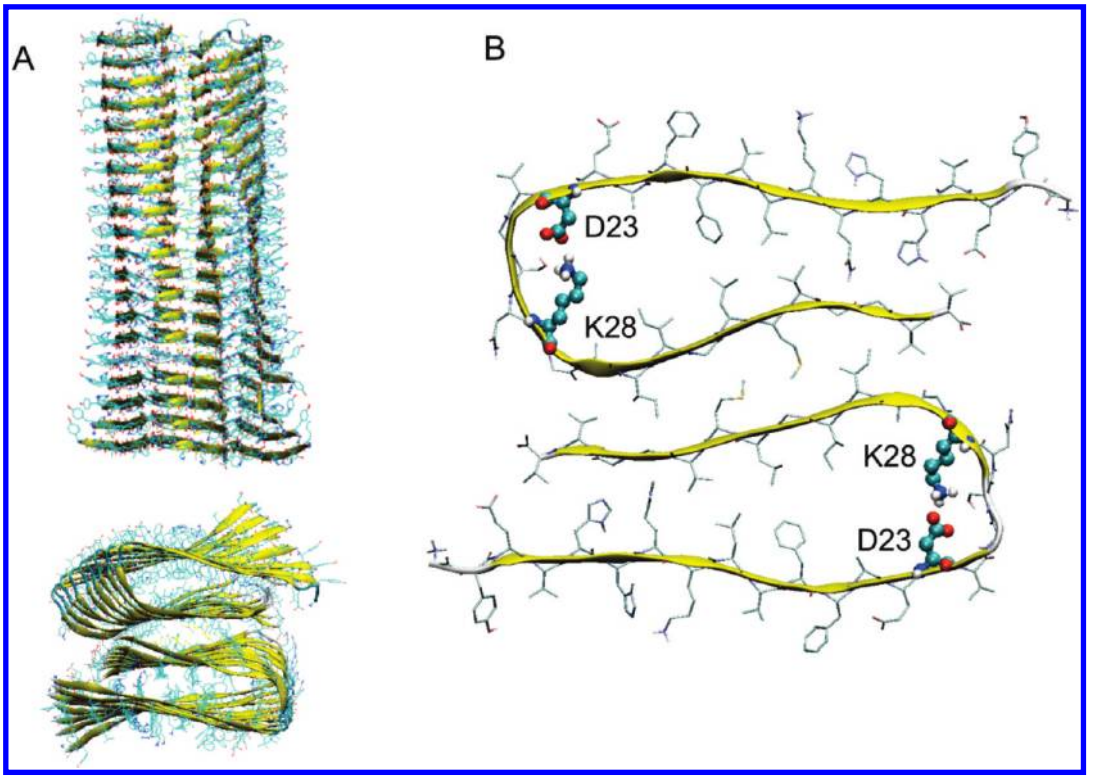

FIGURE 1: Visualization of the molecular structure of the 2-fold symmetric β-peptide amyloid fibril. (A) Side and top views of a 20-layer amyloid fibril after relaxation (*18*, *24*). (B) Detailed view of one layer of the 2-fold amyloid fibril. Residues D23 (aspartate) and K28 (lysine) are highlighted using the CPK representation. These residues are responsible for the formation of the salt bridge stabilizing the β-turn configuration (*19*, *22*) and contribute to the maintenance of the shape of each layer due to both the strong interactions between the side chains and their specific length.

H-bonds). Generally, the amyloid configuration and properties depend primarily on the dense H-bonds network involving the backbone of the polypeptides (*10*), while the side chains play a more pronounced role in the definition of the geometrical details and in the extension of the disordered parts of the structure.

Existing pharmaceutical strategies for curing Alzheimer's disease are based on targeting of the enzymes β- and γ-secretase (*25*) or of the Aβ peptide itself (*3*) in the progression of the disease using antibodies (*26*), peptide-based inhibitors (*26*−*28*), and small molecules (*29*−*32*). Very recently, in vitro studies demonstrated that flavonoids, which are polyphenolic compounds particularly abundant in red wine and green tea, may be useful in targeting the Aβ peptide (*33*, *34*). Moreover, the oral administration of polyphenolic extracts to mice seems to reduce the amyloid plaque burden and to improve memory and cognitive ability (*35*, *36*). Both in vivo and in vitro evidence suggest that flavonoids are able to disrupt Aβ peptide aggregates. A very recent computational experiment showed that morin, one of the most effective flavonoids, is able to bind the ends of an amyloid fibril (*37*), thereby blocking the attachment of an incoming peptide, and can penetrate into the hydrophobic core disrupting the salt bridge [between residues D23 and K28 (for details, see Materials and Methods and Figure 1)]. This is likely the result of the combination of the hydrophobicity, aromaticity, and hydrogen bonding capacity of morin (*37*). Most importantly, this finding implies that the salt bridge may play a key role in stabilizing each layer composing the fibril, promoting the attachment of new units and determining the geometrical and mechanical properties of the overall amyloid fiber or perhaps the plaque. Other information about the effect of the D23−K28 salt bridge on the general stability of these fibrils is provided by the ssNMR data (*19*, *23*) and by atomistic simulations in explicit solvent (*38*) conducted considering different Aβ fibril models with different interpeptide interfaces, and staggering of the N- and C-terminal β-strands along the fibril axis. In all cases, the D23−K28 salt bridges are maintained at 298 K, while mutations of loop residues, in the region of the salt bridge, are found to enhance the flexibility of the fibrils at elevated temperatures (*38*).

All the recent studies mentioned above suggest a significant role of the salt bridge in defining the properties of amyloids (*37*) and call for a systematic investigation of the effect of alterations of the nature of the salt bridge on structural and mechanical properties. Specifically, the geometry of the Aβ peptide amyloid fibril if the salt bridge were disrupted via the replacement of one of its residues or both remains unclear. Furthermore, it is not known whether the mechanical properties of the amyloid fibril would change in the presence of mutations and whether the fibril would retain its stability. Here, we address these questions through series of molecular dynamics simulations conducted to analyze the stability, geometry, and mechanical properties of mutated Aβ peptide amyloid fibrils. The addition of local mutations presents a powerful approach to studying the main factors determining the geometry and mechanical properties of amyloid fibrils. From a medical point of view, such a study could suggest new ideas of targeting possibilities for therapeutic purposes, and it could clarify important details to enhance the mechanical properties of amyloid fibrils that have been also suggested as good candidates for nanotechnology applications.

MATERIALS AND METHODS

Amyloid Fibril Geometry Setup. The amino acid sequence of the 2-fold Aβ(1−40) amyloid fibril is DAEFRHDSGYEVHHQKLVFFAEDVGSNKGAIIGLMVGGVV (*19*). According to the NMR data, the first eight residues exhibit

structural disorder (*19*), and the corresponding coordinates are not yet available. Therefore, only the last 32 amino acids are taken into account to build the fibrils. The first glycine of the sequence (G) will be the reference point (G9) to indicate all the other amino acid positions. On this basis, the aspartate (D) and the lysine (K) forming a salt bridge are in positions 23 and 28, respectively (Figure 1). As shown in previous studies (*24*, *39*), the structure of the relaxed 2-fold symmetric amyloid fibril formed by the Aβ(1−40) peptide can be built through the translation of the coordinates of one layer imposing the typical β-sheet interlayer distance (4.8 Å) and any interlayer twist rotation (*24*). The subsequent relaxation process will drive the fibril toward the optimized interlayer distances and twist angles: the relaxed configuration of a 20-layer fibril (*24*) reported in Figure 1A will be our reference for the evaluation of the changes in the mutated fibrils in terms of geometry, chemistry, and mechanics.

On the basis of the intrinsic structure of amyloid fibrils, the mutations imposed in one layer will be repeated in all the other layers composing the fibril. In this paper, three different mutations will be studied: (i) aspartate (D) in position 23 replaced with glycine (G), (ii) lysine (K) in position 28 replaced with glycine (G), and (iii) both aspartate (D) 23 and lysine (K) 28 replaced with glycine (G). These three mutations will be termed D23, K28, and D23K28, respectively. The coordinates of a single mutated layer have been obtained, substituting only the side chain of one or both of the components of the salt bridge with the single glycine side chain hydrogen. Following the same procedure used for the nonmutated fibrils (*24*, *39*), the layers are then copied and translated along the fibril growth axis, imposing the typical β-sheet interstrand distance (4.8 Å). Therefore, the starting configuration before equilibration consists of layers stacked on top of each other without any interlayer rotation.

Molecular Dynamics Simulations. Atomistic simulations are conducted using the CHARMM molecular dynamics program (*40*). For modeling molecular interactions, the modified all-atom CHARMM19 polar force field is used in conjunction with an effective Gaussian model for the water solvent (*41*). The structural, chemical, and mechanical properties of many biopolymers (including amyloids) are strongly dependent on the chemical environment and on the external conditions, including the specific solvent, pH, temperature, and pressure. The utilization of explicit solvent in molecular dynamics simulations provides a computationally effective yet realistic description of both the solute−solute and solute−solvent interactions (*42*). On the other hand, the presence of solvent molecules typically increases the size of the simulated system (i.e., the number of atoms), resulting in a significant increase in the computational cost. Implicit solvent models have been proposed to reach a good compromise between computational efficiency and scientific accuracy (*41*, *43*). This model includes an effective solvent energy contribution, expressed as a function of the molecular structure and its conformation. The utilization of such a method accelerates the simulation efficiency because it provides an average of the solvent effect and a decrease in the computational cost. Moreover, frictional effects are not included, and the structural reorganization toward the minimum energy average configuration is easier than in the presence of explicit water models. The simplification introduced by continuum solvent models accelerates the sampling of molecular configurations (*44*−*46*), and its success has been confirmed in many fields, such as pK_a calculations, surface electrostatic potentials, solvation free energies, and ligand−receptor binding (*47*−*50*). On the other hand, there has been discussion about the fact that implicit models should be used cautiously, especially with large-scale simulations involving dramatic conformational changes, such as protein folding (*51*), because they may overestimate some energy terms (*50*).

Here, the choice of an implicit solvent model is dictated by the size of the system, and its applicability is supported by earlier studies, which compare the utilization of the explicit and implicit models (*52*). These works were based on the implicit solvent approach and validated against experiments (*18*, *53*). Further, the analysis reported here does not involve changes in the protein conformation, and the interactions driving the equilibration of the studied amyloid fibrils are mainly electrostatic and hydrophobic, which have been demonstrated to be correctly predicted by implicit solvent models (*50*). The relaxation of a 20-layer Aβ amyloid fibril in explicit solvent has been conducted as a preliminary study in our group (results not shown), and from the comparison with the results obtained utilizing the implicit solvent model, the structural and chemical differences between the final configurations did not seem to be significant.

In all cases, the initial structure (obtained as discussed in Amyloid Fibril Geometry Setup) is first minimized to relax the system to a favorable starting configuration and then equilibrated at a constant temperature (using an NVT ensemble) of 300 K. The minimization consists of 10000 steepest descent (SD) steps followed by 50000 adopted basis Newton−Raphson method steps. The subsequent relaxation is performed using the Velocity-Verlet algorithm (VV2) with a time step of 0.001 ps. No constraints are imposed to the system during energy minimization and relaxation. The relaxation is performed until the root mean square deviation (RMSD) of the protein structure remains constant, ensuring that convergence is achieved during the simulation. In all cases, the structures converge in a time range of approximately 2.5 ns.

Mechanical Characterization. The analysis of the nanomechanical properties is performed by conducting constant-force molecular dynamics experiments to simulate the compressive deformation of the protein. The applied load is increased in discrete steps followed by equilibration runs, lasting between 3 and 6 ns (depending on the time scale needed to reach structural equilibrium), to simulate quasi-static loading. According to the loading geometry, the bottom layer of the fibril is fixed and the stress boundary condition is applied by imposing external forces (F), equally distributed over the 64 amino acids composing the top layer, in the direction of the fibril axis. Similar loading conditions have also been applied in experimental studies (*54*).

The applied stress ranges between 0 and 0.13 GPa (in compression) with variable loading increments. The applied stress σ is calculated by considering the rectangular cross-sectional area A of the fibril, via $\sigma = F/A$. As done in ref *18*, the average cross-sectional area (A) of each fibril is estimated according to the average position of the valine (V12) and serine (S26) in the central layer, which is less affected by the entropic effect than the layers composing the tails of the fibril. This choice is justified by the need to have a common calculation method for all the fibrils and to take into account the diverse geometric variations driven by both the local mutations and the thermal fluctuations. The cross-sectional areas correspond to 1644.62, 1475.12, and 1364.16 Å^2 for D23, K28, and D23K28, respectively. In all cases, the fibrils show a significant change in the cross-sectional area with respect to the nonmutated one that features an average area of 1414.32 Å^2 (*18*) (the change in the cross-sectional area is included in the

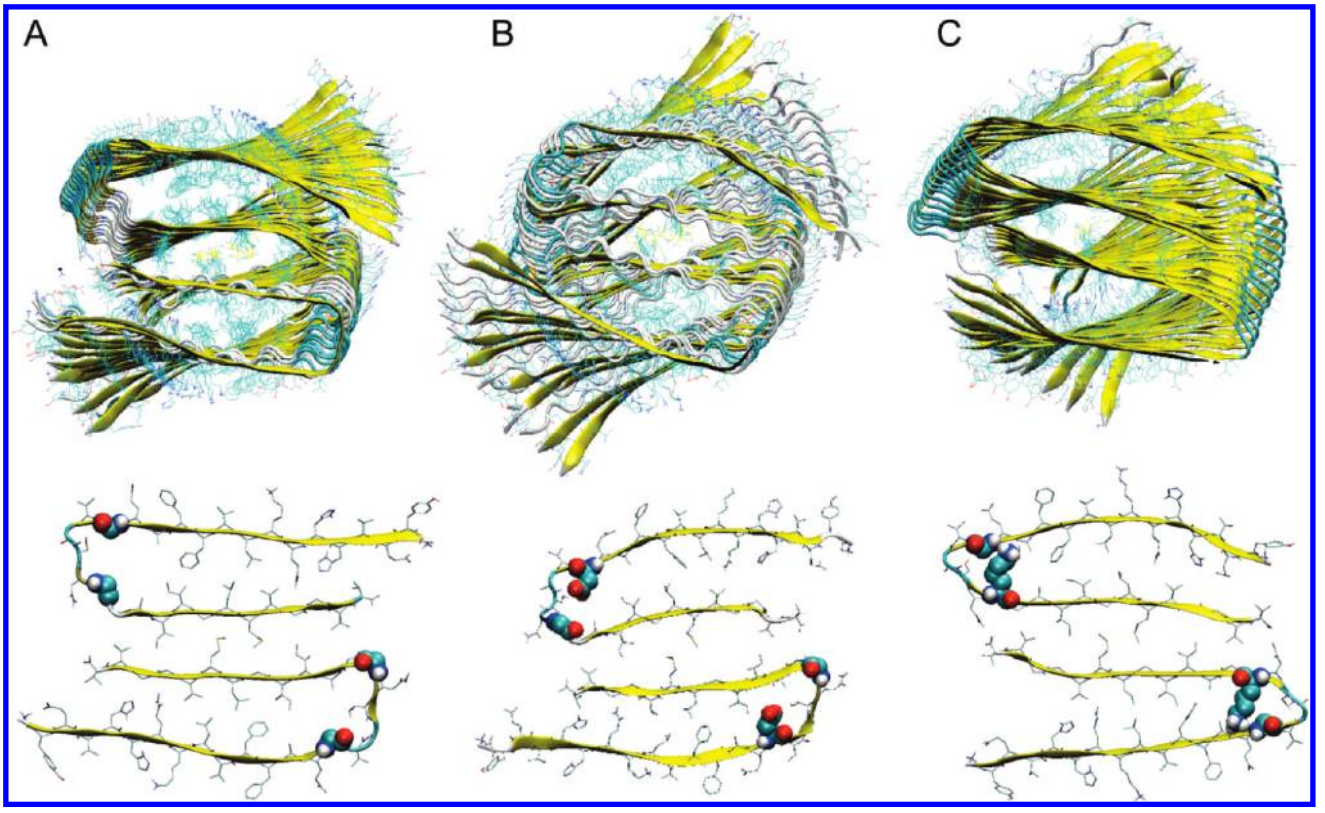

FIGURE 2: Effects of the local mutations on the average twist angle and cross section of the amyloid fibril, for equilibrated structures. The images show the top view of the relaxed fibrils that have none of the components of the salt bridge (D23K28) (A), only the aspartate in position 23 (K28) (B), and only the lysine in position 28 (D23) (C). The positions originally involved in the formation of the salt bridge are represented in CPK visualization to emphasize their location and structure.

mechanical analysis). The corresponding moments of inertia (I) vary from 1.10071×10^{-35} m^4 for the nonmutated fibril to values of 1.07093×10^{-35}, 1.202×10^{-35}, and 1.80123×10^{-35} m^4 for D23K28, K28, and D23, respectively. Each simulation at a particular applied load is conducted until the system reaches the stability and the RMSD converges to a constant value (typically within several nanoseconds). The average displacement of the bottom and top layers is used to calculate the corresponding engineering strain (*18*), which is evaluated when the RMSD has converged.

Geometrical and Chemical Characterization. The interlayer distance (d) of both the relaxed and deformed fibrils is evaluated starting from the average position of the centers in the top and bottom layers, while the twist angle ω is calculated considering the position of amino acid S26 as described in refs *24* and *39*. In all cases, the geometrical parameters are evaluated over the last 0.5 ns relaxation or constant force compression. The corresponding periodicity (ν) can be calculated using the equation $\nu = d_0\Omega/\omega_0$, where $\Omega = 360°$ (*24*, *39*), the periodicity being defined as the length of the amyloid fibril needed to cover a complete twist turn. During compressive loading, changes in the twist angle from ω_0 to ω are observed, and the corresponding winding−unwinding process is estimated calculating the relative variations $\Delta\omega = (\omega - \omega_0)/\omega_0$.

We computed the number of H-bonds along the trajectories using Visual Molecular Dynamics (VMD) (*55*) and imposing a cutoff distance and cutoff angle of 4.0 Å and 40°, respectively. The reported values correspond to the average number of backbone H-bonds during the last 0.5 ns of each simulation. The same software is used to generate all the molecular structures reported in this work.

The error of all the calculated parameters (interlayer distance and twist angle, total energy, number of H-bonds, and stiffness) is estimated considering the corresponding RMSD evaluated over the last 0.5 ns relaxation (this reflects a time scale on which fluctuations of the systems are no longer significant).

RESULTS AND DISCUSSION

Geometric and Structural Characterization of Relaxed Amyloid Fibrils. The relaxed configuration of amyloid fibrils with different mutations is reported in Figure 1A (top and side view) (*18*, *24*). A homogeneous twist angle is found to be distributed throughout the 20 layers composing the fibril. The regularity of each layer is ensured by the salt bridge formed by residues D23 and K28 (Figure 1B). The strong electrostatic interaction and the size of the corresponding side chains impose a specific molecular-level stiffness to each β-turn, reducing the out-of-plane distortions and the effect of thermal fluctuations, which remain evident only in the tails of each polypeptide.

We find that the presence of mutations that cause a complete disruption of the salt bridge has a distinct effect on the geometry of the final configuration, as revealed in Figure 2. The D23K28 fibril contains two mutations per β-turn (i.e., four mutations per layer) and, therefore, neither of the two salt bridge components (Figure 2A). It shows the smallest variation of the twist angle with respect to that of the nonmutated fibril (Figure 3A). In this case, the small glycine amino acids that replace the aspartate and the lysine do not affect the configuration of the neighbor amino acids that form the layer, and the stability depends only on the hydrophobic interactions of the core structure and the H-bond network between adjacent layers. The corresponding cross section

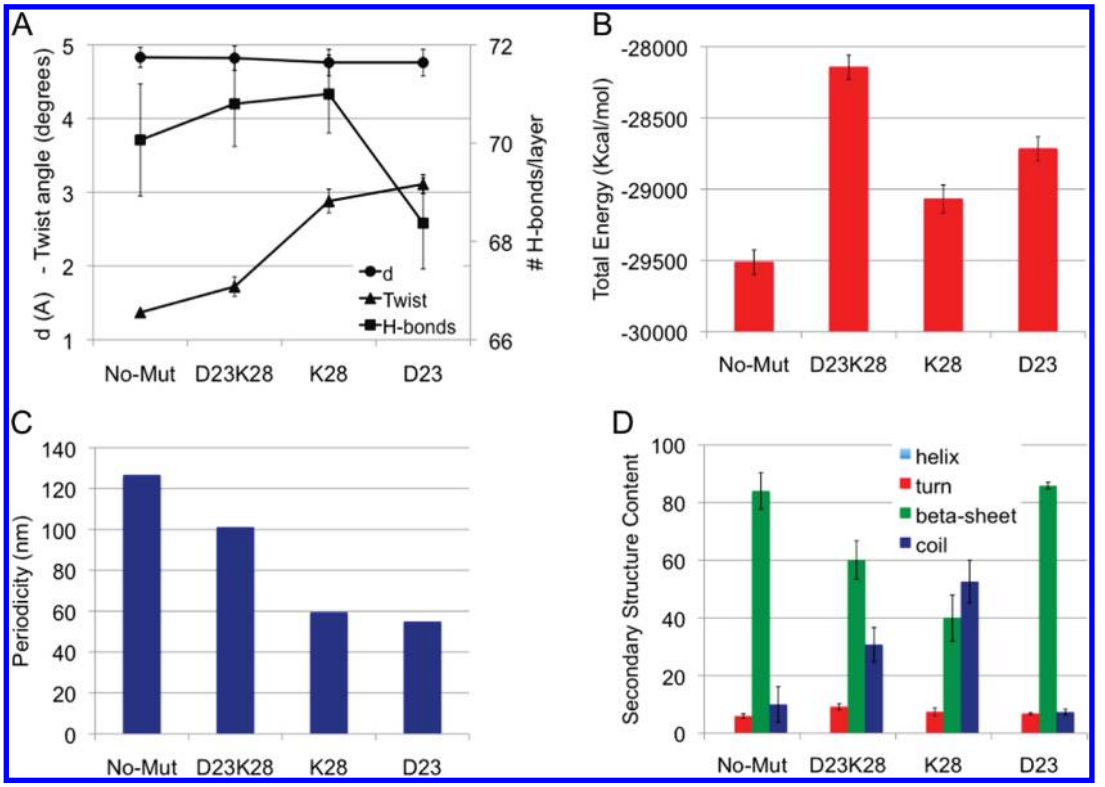

FIGURE 3: Comparison of geometrical, chemical, and energetic properties of the 2-fold amyloid fibrils, with and without mutations. (A) Average interlayer twist angle, interlayer distance *d*, and number of H-bonds per layer for all cases considered. (B) Average total energy of equilibrated fibrils. The results show that all mutated fibrils do not reach the lowest energy level of the nonmutated configuration. (C) Comparison of the periodicity of amyloid fibrils. The results reveal a general trend toward lower periodicities, caused by the increase in the interlayer twist angle as reported in panel A. (D) Secondary structure content for the reference case and mutations. In all cases, the structural parameters fluctuate around the average values and the corresponding estimated errors for the interlayer twist angle and distance, for the number of H-bonds, and for the total energy vary in the ranges of 1−8%, 2−4%, 1.3−1.7%, and 0.2−0.4%, respectively.

shows a planar extended configuration, and no specific interactions involve the side chains of the amino acids composing the same β-turn. For the same reason, the bent part of the β-turn, slightly distorted in the nonmutated fibril, appears on average more regular during the relaxation process.

A larger change in the twist angle is observed when the salt bridge is not formed, but when at least one of the two components is still present (Figure 2B,C). Without its partner in forming the salt bridge, the remaining charged side chain determines the increasing number of interlayer interactions and twist angle (Figure 3). Both the aspartate (Figure 2B) and the lysine (Figure 2C) when freed from the salt bridge interact with the amino acids that belong to the same β-turn and thereby drive significant distortions of each layer. In particular, the aspartate residue tends to orient its side chain toward the center of the β-turn to form a new H-bond with the hydroxyl group that belongs to the side chain of residue S26. This interaction results in a much distorted β-turn, and overall in a more disordered amyloid fibril that has a decreased β-sheet content (Figure 3D). The effect of the lysine (Figure 2C) is even more pronounced. It has a charged, flexible side chain that is generally oriented toward the center of the β-turn and in particular toward the backbone oxygen of residue A21. The reason for this orientation is related to both the steric constraint and the tendency of the charged side chain to escape the hydrophobic inner core of the fibril that does not allow it to orient in the opposite direction. The lysine extension and interactions result in a narrower β-turn and, in a manner different from the other cases, in an almost perfect alignment of the two arms.

The structural differences observed among the fibrils reported in Figure 2 suggest that the main contributions to the stability are the hydrophobic interactions, H-bonding, and salt bridge formation. Figure 3 shows the average geometrical parameters extracted from the amyloid fibrils considered here. The presence of a salt bridge makes the β-turn extremely stiff and stable, and a small interlayer twist angle (1.32°) is necessary to increase the number of H-bonds and to optimize the intermolecular distances (Figure 3A). When one of the components of the salt bridge is no longer present, the β-turns are more deformed and especially the out-of-plane distortions allow wider movements that increase that twist angle, change the H-bond network density, and change the corresponding distribution of secondary structure content. In particular, the largest twist angle (3.11°) is due to the effect of the long and charged side chain of the lysine group in the D23 fibril (Figure 3A). Finally, when the sequence lacks both the components of the salt bridge, there are no additional free side chains or other interactions that drive significant distortions, and as a result, only a relatively small twist angle (1.72°) can be achieved to increase the number of H-bonds and make the structure stable.

Even though all mutated fibrils become more stable in an attempt to balance the loss of the salt bridge, their energy remains higher than those of the corresponding nonmutated versions (Figure 3B). In particular, the highest energy corresponds to the structure with two mutations per β-turn, confirming its inability to optimize further the intermolecular distances and interactions. From the analysis of the average secondary structure (Figure 3D), it is evident that the high β-sheet content characteristic of the

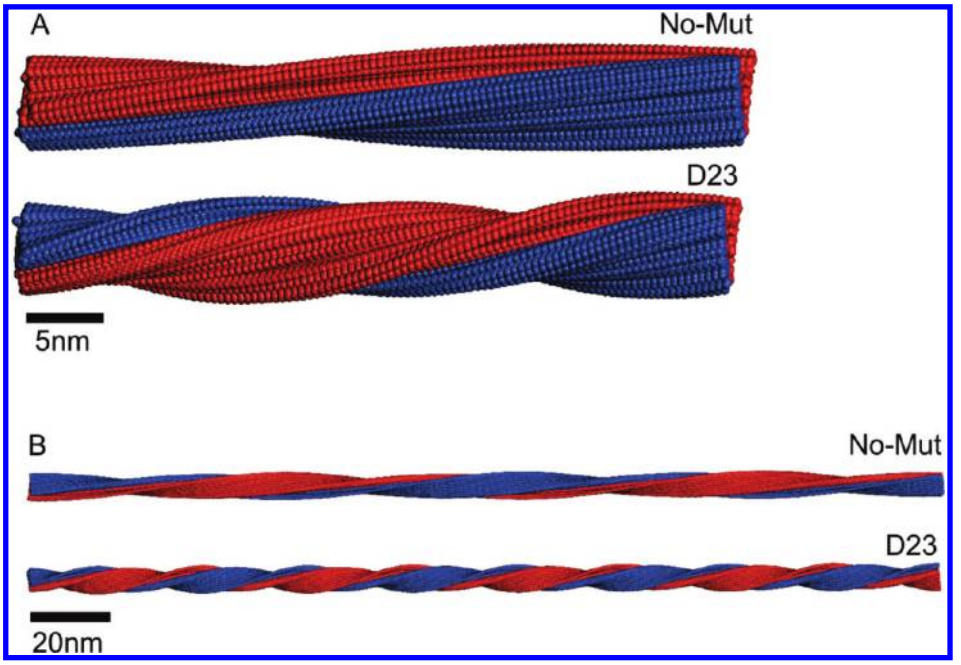

FIGURE 4: Comparison of the periodicities of the nonmutated and D23 fibril at the mesoscale (the D23 case is chosen here because it shows the most severe change in the fibril periodicity among all mutations considered). Panels A and B show fibrils with lengths of ≈48 nm (100 layers) and ≈230 nm (500 layers), respectively. In both cases, the nonmutated fibril and the D23 fibril are shown in the top and bottom images, respectively. The two protein parts that compose each fibril are colored red and blue to enhance the twist angle and the differences between the periodicities. The severe increase in the twist angle per layer, and as a result the decrease in periodicity, is evident from the visualizations.

nonmutated fibrils is reached only in the D23 case, where the remaining lysine plays a strong role in driving the movements of the layers. Even though in this case the fibril features an average number of H-bonds per layer that is slightly lower than those of the other mutated fibrils, the presence of the lysine and the corresponding strong interactions make the formed H-bonds efficient in terms of the formation of ordered β-sheet layers, resulting in a high β-sheet content and a small percentage of coil configuration. This arrangement can only partially repair the lack of the complete salt bridge, and the corresponding energy is higher than that of the nonmutated fibril. In the other two cases, we observe an increase in the β-sheet content and a decrease in the coil content; the side chain groups cannot promote further stabilization and ordering of the structure even though the number of H-bonds is slightly higher.

Among the mutated fibrils, the K28 case becomes the most stable, showing also a relatively large number of H-bonds. This apparent level of stability may be related to the high flexibility of the layer that makes possible out-of-plane motions, making the fibril more distorted, but allowing the optimization of interactions even though the fibril is in a coil configuration. Altogether, these observations suggest the importance of electrostatic interactions in the promotion of the stability of amyloid fibrils and show that if on one hand the twist motion represents a key structural tool for optimizing the total energy, on the other the formation of ordered layers is strictly related to the intralayer interactions and to the intrinsic rigidity of each β-unit.

The change in the geometric properties of the fibrils due to the local mutations results in all cases in a decrease in the corresponding periodicity as shown in Figure 3C. According to a proposed model (*24*, *39*), the geometric information concerning the interlayer distance and twist angle can be used to build fibers of any length. Figure 4 reports snapshots of the geometry of amyloid β-peptide fibrils with a length of ≈48 nm (panel A) and ≈230 nm (panel B). In both panels, a fibril with no mutations (top) and a D23 fibril (bottom) are shown for comparison. The difference in periodicity is evident, where the D23 mutation causes an ≈43.4% decrease in periodicity.

To enable a further analysis of the local motions and distortions, we report the average distance between each α-carbon in the mutated fibrils and the corresponding position in the nonmutated relaxed Aβ peptide (Figure 5). According to the used code, the red color indicates a higher mobility and the largest distances are observed in the K28 and D23 fibrils, where the remaining part of the salt bridge directs the motions of the overall layer. The D23K28 fibril shows a still large but homogeneous distribution of the local distances along each β-turn, confirming the lack of specific groups able to drive and localize further motions.

Mechanical Tests and Characterization. We continue the analysis with a study of the mechanical properties of amyloid fibrils with different mutations. Compressive loading tests are performed on the three mutated fibrils, to shed light on the effect of the salt bridge disruption on the mechanical properties of the Aβ peptide fibrils. It is noted that in the nonmutated configuration, in both experiment and simulation, these fibrils showed a very high Young's modulus and a remarkable bending stiffness corresponding to 12.43 GPa and 13.2×10^{-26} N m^2, respectively (*10*, *17*, *18*). The stress−strain analysis of the D23K28, K28, and D23 systems reveals that in the last two cases, the elastic modulus decreases to 4.47 ± 0.52 and 4.53 ± 0.72 GPa, respectively, while the corresponding bending stiffness becomes 5.37×10^{-26} and 8.159×10^{-26} N m^2, respectively. In the D23K28 fibrils, we find that the Young's modulus increases to 19.09 ± 5.55 GPa while the bending stiffness reaches a value of 2.044×10^{-25} N m^2.

These significant changes in the mechanical properties can be explained on the basis of the molecular rearrangements of the structure during the loading and the resulting pathway that each side chain follows. Interestingly, as already observed in mechanical tests of the nonmutated fibril (*18*), the compression mode is coupled with a twisting movement, which is evident from the

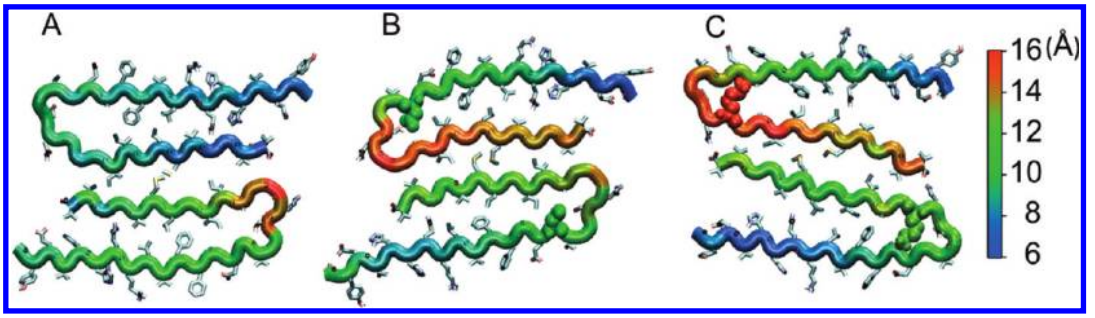

FIGURE 5: Average deviation of each α-carbon from the original position in the nonmutated, relaxed configuration: D23K28 (A), K28 (B), and D23 (C). In panels B and C, the remaining part of the salt bridge (an aspartate and a lysine residue, respectively) is highlighted using the CPK representation. The corresponding neighbors show a relatively high mobility with respect to the nonmutated fibril.

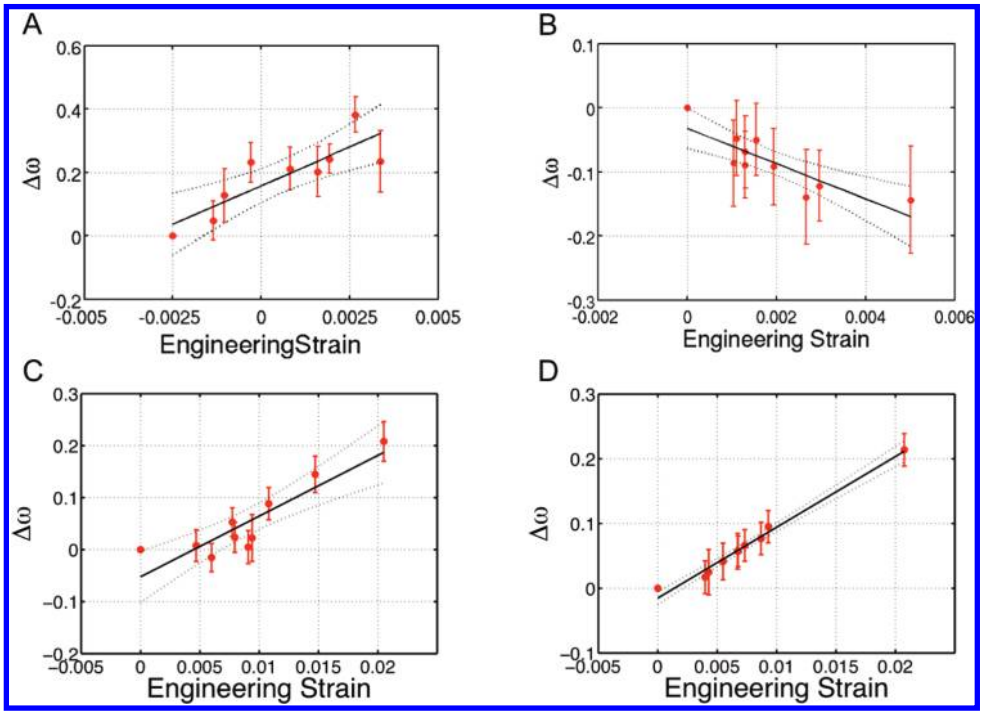

FIGURE 6: Coupling of compression and twisting mode under axial deformation of amyloid fibrils. The panels report the variation of the twist angle as a function of the measured engineering strain for the nonmutated fibril (panel A, data as reported in ref *18*), D23K28 (B), K28 (C), and D23 (D). The analysis reveals that for all cases but D23K28, the twist angle increases as the strain increases. The error bars correspond to the RMSD of the average interlayer twist angle calculated along the last 0.5 ns relaxation. The linear fit is here used only to indicate the general trend, and the dashed lines define the confidence interval.

calculation of variation of the average interlayer twist angle (Figure 6). In particular, in the K28 and D23 cases, we observe an increase in the average twist angle, which implies a winding rearrangement process during compressive deformation (Figure 6C,D). In the D23K28 fibril, however, compression causes an opposite variation of the twist angle. This suggests that during compressive loading the fibril experiences an unwinding process (Figure 6B). Considering the atomistic details, the variation of the twist angle is in all cases combined with the increase in H-bond network density (Figure 8A,B). Such an increment is caused by both the smaller interlayer distances imposed by the loading and the twisting mode that is driven by the relatively strong electrostatic interactions due to the partial charge distribution among the atoms (in particular H, O, and N).

The comparison of the twist angle variation between the mutated and nonmutated fibrils shows that the mutation in general weakens the ability of the fibril to rearrange the internal structure through the twisting mode. For example, the twist angle change at 0.4% strain is ≈23% in the nonmutated fibril, ≈7% in the K28 fibril, and ≈2% in the D23 fibril. In the D23K28 case, the variation of the twist angle for a strain in the range of 0.5% corresponds to approximately −14%. This result correlates well with our finding of a larger Young's modulus in the absence of both salt bridge components. In this case, the fibril is rather stiff, and the increase in the twist angle under loading drives the mechanical response.

We report the atomistic details of the interactions before and during the compression in the D23 fibril (Figure 7). In the relaxed configuration, as already observed, K28 stabilizes the entire *β*-turn interacting with A21 as shown in Figure 7A. During the compression, this interaction is still kept, but new H-bonds are formed between the NH_3^+group of each lysine and the side chain of the corresponding lysine belonging to the lower layer (Figure 7B). This new interaction, due to the external loading and the repulsion between the two NH_3^+ groups of the two interacting lysine residues, drives the winding motion observed for this structure, which in the reported case is ≈7% at 0.8%

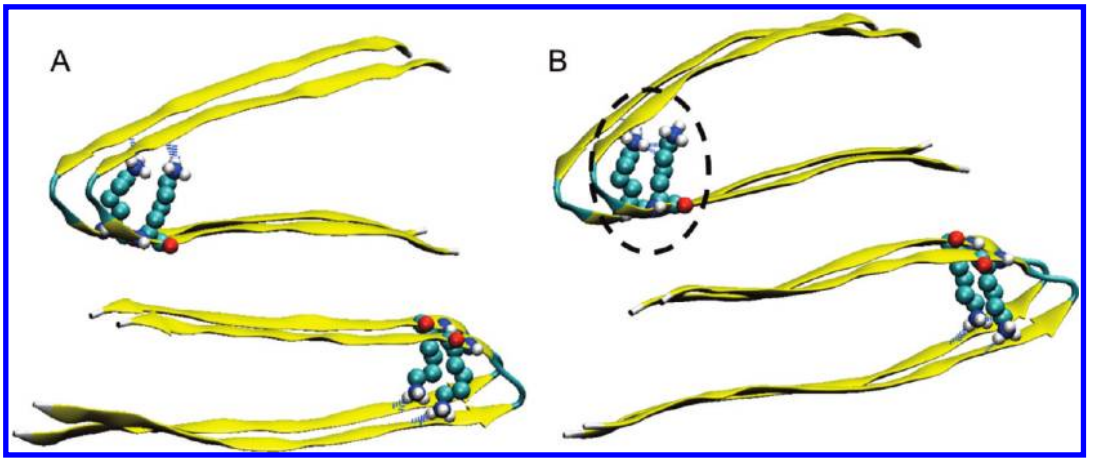

FIGURE 7: Twist angle variation during compression loading. Panels A and B show the atomistic detail of a 2-layer unit of the relaxed and compressed D23 fibril (at 0.8% strain). After the relaxation, the lysine side chain is mainly oriented toward the opposite arm of the β-turn forming H-bonds with the backbone oxygen of A21 (see also Figure 2). (B) During the compression, the long and flexible side chain of the lysine moves out of the β-turn plane, keeping the previous interactions and initiating new H-bonds with the side chain of the corresponding lysine in the lower layer. This new interaction is mainly responsible for the measured variation of the twist angle. In both cases, the backbone of the two layers is represented using the "New Cartoon" representation in VMD (*55*), while the lysine structure is emphasized using the CPK visualization.

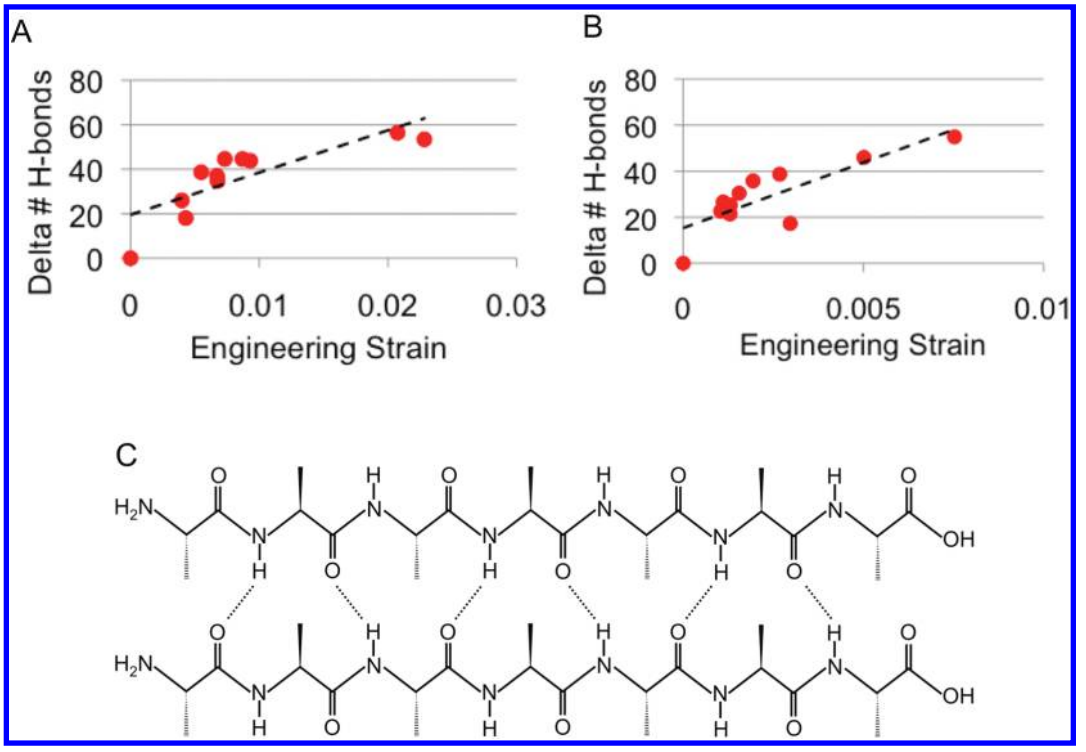

FIGURE 8: Molecular rearrangement during the compressive loading. (A and B) Variation of the average number of H-bonds formed by the backbone as a function of the measured engineering strain in the D23 (A) and D23K28 (B) fibrils. (C) Schematic of the antiparallel β-sheet configuration, illustrating the relatively large H-bond lengths.

strain. In the D23K28 case, the largest measured twist angle variation is approximately −14% and corresponds to ≈0.5% strain. In Figure 8B, the variation of the number of H-bonds formed by the backbone of the D23K28 fibril is reported as a function of the engineering strain. The corresponding plot of the D23 fibril is shown in Figure 8A for comparison. In these two cases, as well as for the nonmutated (*18*) and K28 fibrils, the compressive loading causes an increase in H-bond network density. In the D23K28 case, the larger number of H-bonds is coupled with an unwinding of the fibril. The replacement of both the long side chains, D23 and K28, with the small glycine residues makes the backbone interactions drive the molecular rearrangement under compressive loading. The β-sheets composing the amyloid fibrils are parallel, and therefore, the H-bond lengths are on average relatively large, because of the reciprocal orientation of the oxygen, nitrogen, and hydrogen atoms in neighboring layers. In this scenario, the compressive loading causes in-plane movements aimed solely at maximizing the local electrostatic interactions of the backbone (Figure 8C).

Mechanical Failure in Compression. Our understanding of the molecular mechanisms determining the mechanical responses and in particular the failure of materials is crucial to identifying the link between the structure and the behavior of materials. In the specific case of amyloid fibrils, this insight is useful for identifying the particular structural elements driving the molecular rearrangements and finally the failure of the fibril.

We monitored the mechanical response of all three mutated fibrils until failure by progressively increasing the loading. The mechanical tests performed on the nonmutated Aβ(1−40) amyloid fibrils [as reported in an earlier study (*56*)] showed that the failure mechanism is initiated by the buckling response of each fibril and could be associated with a concomitant variation of the number of H-bonds. We find that the mutations do not change the failure mechanism of the fibril, and in all cases, we observe a buckling of the fibril quickly resulting in sudden failure.

The D23 fibril fails when a $>2.3\%$ strain is reached. In this case, a relatively small strain is enough to cause the failure, likely because the relaxed fibril already features a very high interlayer twist angle (on average 3.11°), and further possible molecular rearrangements in response to the applied stress are limited without them causing major disruptions of the H-bond network. The D23K28 fibril fails at strains higher than 0.7%. This severe change of the failure point also confirms the higher rigidity introduced by the double mutation, and the loss of the capacity of this fibril to rearrange the internal structure through twisting motions. The K28 mutation requires the highest applied stress to be broken. The failure occurs at ≈2.8% strain, when the applied stress reaches a value of 0.13 GPa. The highest energy required by this fibril is related to its higher stability (Figure 3) when compared with those of the other mutations. The K28 fibril shows the best rearrangement after the mutation is introduced: even though it features the lowest β-sheet content, its twist angle still allows significant optimization of the inter- and intramolecular distances during compressive loading. This is also confirmed by the fact that its failure point is very close to that observed for the nonmutated fibril (*56*). All these observations suggest that the twist motion could serve as a key tool to ensure the mechanical stability featured by this class of materials.

CONCLUSION

The identification of the molecular details responsible for defining the stability and properties of amyloid fibrils and promoting their growth is crucial for biomedical applications and for further progress in improving efficient Alzheimer's disease treatments. Great interest is focused on the ability of small molecules, for example, morin (*37*) and ibuprofen (*57*), to penetrate the dense and stiff structure of amyloid fibrils, to interact with specific groups composing the side chains, to promote their destabilization, and, ultimately, to reduce their toxicity. On the basis of this perspective, an understanding of the molecular mechanisms and interactions involving some key local points in the structure is crucial for further experimental studies with direct biomedical applications. In this context, the results presented here demonstrate that the presence of the salt bridge is important for the stability, geometry, and mechanical behavior of these amyloid fibrils. Our observation of a decrease in the amyloid fibril periodicity of up to ≈43%, and the prediction of extreme variations of the Young's modulus of up to ≈154% (Figure 3), could be seen as a challenge to experimentalists. As also suggested by other works, the salt bridge network and its effect on the amyloid activity are two of the requirements for promoting the growth of the fibrils and/or the formation of complexes with other ligands and proteins (*58*).

The results presented in this paper could be extended to the several polymorphic states of the Aβ (oligo) peptides, which have been studied both experimentally (*23*) and theoretically (*59*−*61*) and for which different models have been proposed (*22*, *62*, *63*). In particular, the prediction of the mechanical properties as a function of local mutations, could be expanded toward a more general study involving the presence of ions (*60*), and of different chemical environments determined by variations in solvent, pH, pressure, and temperature (*64*, *65*). Such analyses could turn out to be very useful given the mixed population expected for these particular species of amyloids and could help in the prediction of the corresponding behavior from a chemical, pathological, and mechanical point of view. Furthermore, the first eight amino acids in the amyloid molecular model [which have been observed in ssNMR experiments (*19*, *23*) but are not structurally characterized, given their disorder] could be included in future studies perhaps by applying alternative methods such as replica exchange molecular dynamics, to quantify their contribution to the general properties of these fibrils.

From a more general perspective, the cases reported in this work show the influence of the side chains on the properties of the amyloid fibrils, confirming that the overall amyloid structure depends on the sequence backbone, but the properties and relative positions of the side chains can significantly affect the fibril's geometry and mechanics. Furthermore, previous experimental work (*66*) shows the importance of the formation of the D23−K28 salt bridge in driving the kinetics of fibrillogenesis. An Aβ(1−40) peptide containing a lactam bridge between side chains D23 and K28 aggregates 1000-fold faster than a normal fibril without showing the typical lag phase of amyloid aggregation in which no fibrils are formed, and that is followed by rapid polymerization of the peptide into fibrils (*66*). Therefore, the influence of the side chain interactions and positions can be exploited to tune the aggregation rate, the chemistry, and the mechanics of amyloid fibrils, opening new perspectives for the improvement of drug design in Alzheimer's disease therapy.

The applications of amyloid fibrils require the consideration of the controversial issue of the amyloid neurotoxicity (*67*, *68*). On one hand, it has been shown that different types of soluble amyloid oligomers have a common structure and share a common mechanism of toxicity (*69*). However, on the other hand, experimental studies revealed that fibril formation is necessary to induce Aβ peptide toxicity (*70*). From an engineering point of view, the utilization of the point mutations could be used to tune the structural and mechanical properties of the amyloid fibrils, enhancing the range of possible applications of amyloid materials in nanotechnology. Local mutations, combined with changes in the chemical environment and with external perturbation, would render amyloids interesting mechanomutable materials (*71*).

ACKNOWLEDGMENT

We declare no conflict of interest of any sort. All authors have contributed equally to the research and the writing of this paper.

REFERENCES

1. Alzheimer's Association (2009) Alzheimer's disease facts and figures. *Alzheimer's Dementia* 234–270.
2. Citron, M. (2010) Alzheimer's disease: Strategies for disease modification. *Nat. Rev. Drug Discovery 9*, 387–398.
3. Hardy, J. A., and Selkoe, D. J. (2002) The Amyloid Hypothesis of Alzheimer's Disease: Progress and Problems on the Road to Therapeutics. *Science 297*, 353–356.
4. Nelson, R..; et al. (2005) Structure of the cross-β spine of amyloid-like fibrils. *Nature 435*, 773–778.

5. Goldschmidt, L..; et al. (2010) Identifying the amylome, all proteins capable of forming amyloid-like fibrils. *Proc. Natl. Acad. Sci. U.S.A. 107*, DOI: 10.1073/pnas.0915166107 .
6. Chiti, F., and Dobson, C. M. (2006) Protein misfolding, functional amyloid, and human disease. *Annu. Rev. Biochem. 75*, 333–366.
7. Fowler, D. M..; et al. (2007) Functional amyloids: From bacteria to humans. *Trends Biochem. Sci. 32*, 217–224.
8. Maji, S. K..; et al. (2007) Functional amyloids as natural storage of peptide hormones in pituitary secretory granules. *Science 325* (5938), 328–332.
9. Dobson, C. M. (2003) Protein folding and misfolding. *Nature 426*, 884–890.
10. Knowles, T. P..; et al. (2007) Role of intermolecular forces in defining properties of protein nanofibrils. *Science 318* (5858), 1900–1902.
11. Fandrich, M., Fletcher, M. A., and Dobson, C. M. (2001) Amyloid fibrils from muscle myoglobin. *Nature 410*, 165–166.
12. Reches, M., and Gazit, E. (2005) Self assembly of peptide nanotubes and amyloid-like structures by charged termini capped diphenylalanine peptide analogous. *Isr. J. Chem. 45*, 363–371.
13. M Yemini, M. R., Risphon, J., and Gazit, E. (2005) Novel electrochemical biosensing platform using self-assembled peptide nanotubes. *Nano Lett. 5*, 183–186.
14. Cherny, I., and Gazit, E. (2008) Amyloids: Not only pathological agents but also ordered nanomaterials. *Angew. Chem., Int. Ed. 47*, 4062–4069.
15. Gazit, E. (2007) Use of biomolecular templates for the fabrication of metal nanowires. *FEBS J. 274*, 317–322.
16. Knowles, T. P. J..; et al. (2010) Nanostructured films from hierarchical self-assembly of amyloidogenic proteins. *Nat. Nanotechnol. 5*, 204–207.
17. Smith, J. F..; et al. (2006) Characterization of the nanoscale properties of individual amyloid fibrils. *Proc. Natl. Acad. Sci. U.S.A. 43* (103), 15806–15811.
18. Paparcone, R., Keten, S., and Buehler, M. J. (2010) Atomistic simulation of nanomechanical properties of Alzheimer's Aβ(1−40) amyloid fibrils under compressive and tensile loading. *J. Biomech. 43* (6), 1196–1201.
19. Petkova, A. T..; et al. (2002) A structural model for Alzheimer's β-amyloid fibril based on experimental constraints from solid state NMR. *Proc. Natl. Acad. Sci. U.S.A. 99* (26), 16742–16747.
20. Buchete, N. V., Tycko, R., and Hummer, G. (2005) Molecular dynamics simulations of Alzheimer's β-amyloid protofilaments. *J. Mol. Biol. 353*, 804–821.
21. Tarus, B., Straub, J. E., and Thirumalai, D. (2006) Dynamics of Asp23-Lys28 Salt-Bridge Formation in Aβ(10−35) Monomers. *J. Am. Chem. Soc. 128* (50), 16159–16168.
22. Ma, B., and Nussinov, R. (2002) Stabilities and conformations of Alzheimer's β-amyloid peptide oligomers (Aβ16−22, Aβ16−35, and Aβ10−35): Sequence effects. *Proc. Natl. Acad. Sci. U.S.A. 99*, 14126–14131.
23. Paravastu, A..; et al. (2008) Molecular structural basis for polymorphism in Alzheimer's β-amyloid fibrils. *Proc. Natl. Acad. Sci. U.S.A. 105* (47), 18349–18354.
24. Paparcone, R., Sanchez, J., and Buehler, M. J. (2010) Comparative study of polymorphous Alzheimer's Aβ(1−40) amyloid nanofibrils and microfibers. *J. Comput. Theor. Nanosci. 7*, 1279–1286.
25. Barton, D. M., and Albright, C. F. (2008) Therapeutic strategies for Alzheimer's disease. *Mol. Neurobiol. 37*, 171–186.
26. Ramakrishnan, M..; et al. (2009) Surface plasmon resonance binding kinetics of Alzheimer's disease amyloid β peptide-capturing and plaque-binding monoclonal antibodies. *Biochemistry 48*, 10405–10415.
27. Takahashi, T., Ohta, K., and Mihara, H. (2010) Rational design of amyloid β peptide-binding proteins: Pseudo-Aβ β-sheet surface presented in green fluorescent protein binds tightly and preferentially to structured Aβ. *Proteins: Struct., Funct., Bioinf. 78*, 336–347.
28. Fradinger, E. A..; et al. (2008) C-Terminal peptides coassemble into Aβ(42) oligomers and protect neurons against Aβ42-induced neurotoxicity. *Proc. Natl. Acad. Sci. U.S.A. 105*, 14175–14180.
29. Gestewicki, J. E., Crabtree, G. R., and Graef, I. A. (2004) Harnessing chaperones to generate small-molecule inhibitors of amyloid β aggregation. *Science 306*, 865–869.
30. McLaurin, J., Kierstead, M. E., Brown, M. E., and Hawkes, C. A. et al. (2006) Cyclohexanehexol inhibitors of Aβ aggregation prevent and reverse Alzheimer phenotype in a mouse model. *Nat. Med. 12*, 801–808.
31. Liu, R..; et al. (2005) Trehalose differentially inhibits aggregation and neurotoxicity of β-amyloid 40 and 42. *Neurobiol. Dis. 20*, 74–81.
32. Forloni, G..; et al. (2001) Anti-amyloidogenic activity of tetracyclines: Studies in vitro. *FEBS Lett. 487*, 404–407.
33. Ono, K..; et al. (2006) Antiamyloidogenic effects of antioxidants: Implications for the prevention and therapeutics of Alzheimer's disease. *Biochim. Biophys. Acta 1762*, 575–586.
34. Ono, K..; et al. (2003) Potent anti-amyloidogenic and fibril-destabilizing effects of polyphenols in vitro: Implications for the prevention and therapeutics of Alzheimer's disease. *J. Neurochem. 87*, 172–181.
35. Ho, L..; et al. (2009) Heterogeneity in red wine polyphenolic contents differentially influences Alzheimer's disease-type neuropathology and cognitive deterioration. *J. Alzheimer's Dis. 16*, 59–72.
36. Wang, J..; et al. (2008) Grapederived polyphenolics prevent Aβ oligomerization and attenuate cognitive deterioration in a mouse model of Alzheimer's disease. *J. Neurosci. 28*, 6388–6392.
37. Lemkul, A., and Bevan, D. (2010) Destabilizing Alzheimer's Aβ42 Protofibrils with Morin: Mechanistic Insights from Molecular Dynamics Simulations. *Biochemistry 49* (18), 3935–3946.
38. Buchete, N.-V., and Hummer, G. (2007) Structure and Dynamics of Parallel β-Sheets, Hydrophobic Core, and Loops in Alzheimer's Aβ Fibrils. *Biophys. J. 97*, 3032–3039.
39. Paparcone, R., and Buehler, M. J. (2009) Microscale structural model of Alzheimer Aβ(1−40) amyloid fibril. *Appl. Phys. Lett. 94*, 243904–243906.
40. Brooks, B. R..; et al. (1983) CHARMM: A program for macromolecular energy, minimization, and dynamics calculations. *J. Comput. Chem. 4* (2), 187–217.
41. Lazaridis, T., and Karplus, M. (1999) Effective energy function for proteins in solution. *Proteins: Struct., Funct., Bioinf. 35* (2), 133–152.
42. Nymeyer, H., and Garcia, A. E. (2003) Simulation of the folding equilibrium of α-helical peptides: A comparison of the generalized Born approximation with explicit solvent. *Proc. Natl. Acad. Sci. U.S.A. 100* (24), 13934–13939.
43. Lazaridis, T., and Karplus, M. (1997) "New view" of protein folding reconciled with the old through multiple unfolding simulations. *Science 278* (5345), 1928–1931.
44. Best, R. B..; et al. (2007) Effect of flexibility and cis residues in single-molecule FRET studies of polyproline. *Proc. Natl. Acad. Sci. U.S.A. 104* (48), 18964–18969.
45. Paci, E., and Karplus, M. (2000) Unfolding proteins by external forces and temperature: The importance of topology and energetics. *Proc. Natl. Acad. Sci. U.S.A. 97* (12), 6521–6526.
46. Paci, E., and Karplus, M. (1999) Forced unfolding of fibronectin type 3 modules: An analysis by biased molecular dynamics simulations. *J. Mol. Biol. 288* (3), 441–459.
47. Onufriev, A., Bashford, D., and Case, D. (2000) A modification of the generalized born model suitable for macromolecules. *J. Phys. Chem. B 104*, 3712–3720.
48. Gallicchio, E., Zhang, L., and Levy, R. (2002) The sgb/np hydration free energy model based on the surface generalized born solvent reaction field and novel non-polar hydration free energy estimators. *J. Comput. Chem. 23* (5), 517–529.
49. Zhou, R..; et al. (2001) New linear interaction method for binding affinity calculations using a continuum solvent model. *J. Phys. Chem. B 105*, 10388–10397.
50. Zhou, R. (2003) Free Energy Landscape of Protein Folding in Water: Explicit vs. Implicit Solvent. *Proteins 53*, 148–161.
51. Zhou, R. H., and Berne, B. J. (2002) Can a continuum solvent model reproduce the free energy landscape of a β-hairpin folding in water? *Proc. Natl. Acad. Sci. U.S.A. 99* (20), 12777–12782.
52. Qin, Z., and Buehler, M. (2010) Structure and dynamics of human vimentin intermediate filament dimer and tetramer in explicit and implicit solvent models. *J. Mol. Model.* (in press) DOI: 10.1007/s00894-010-0696-6.
53. Qin, Z., Kreplak, L., and Buehler, M. (2009) Hierarchical Structure Controls Nanomechanical Properties of Vimentin Intermediate Filaments. *PLoS One 4* (10), No. e7294.
54. Hansma, H. G..; et al. (2000) Probing biopolymers with the atomic force microscope: A review. *J. Biomater. Sci., Polym. Ed. 11* (7), 675–683.
55. Humphrey, W., Dalke, A., and Schulten, K. (1996) VMD: Visual Molecular Dynamics. *J. Mol. Graphics 14*, 33–38.
56. Paparcone, R., and Buehler, M. J. (2010) Failure of Alzheimer's Aβ(1−40) amyloid nanofibrils under compressive loading. *JOM 62* (4), 64–68.
57. Raman, E. P., Takeda, T., and Klimov, D. K. (2009) Molecular dynamic simulations of ibuprofen binding to Aβ peptides. *Biophys. J. 97*, 2070–2079.
58. Luo, J..; et al. (2010) Silico Analysis of the Apolipoprotein E and the Amyloid β Peptide Interaction: Misfolding Induced by Frustration of the Salt Bridge Network. *PLoS Comput. Biol. 6* (2), No. e1000663.

59. Miller, Y., Ma, B., and Nussinov, R. (2009) Polymorphism of Alzheimer's Aβ17−42 (p3) Oligomers: The Importance of the Turn Location and Its Conformation. *Biophys. J. 97*, 1168–1177.
60. Miller, Y., Ma, B., and Nussinov, R. (2010) Zinc ions promote Alzheimer Aβ aggregation via population shift of polymorphic states. *Proc. Natl. Acad. Sci. U.S.A. 107* (21), 9490–9495.
61. Miller, Y., Ma, B., and Nussinov, R. (2010) Polymorphism in Alzheimer Aβ Amyloid Organization Reflects Conformational Selection in a Rugged Energy Landscape. *Chem. Rev. 110*, 4820–4838.
62. Petkova, A. T., Yau, W. M., and Tycko, R. (2006) Experimental constraints on quaternary structure in Alzheimer's β-amyloid fibrils. *Biochemistry 45*, 498–512.
63. Lührs, T..; et al. (2007) Structure of Alzheimer's amyloid-β (1−42) fibrils. *Proc. Natl. Acad. Sci. U.S.A. 102*, 17342–17347.
64. Shen, C.-L., and Murphy, R. M. (1995) Solvent effects on self-Assembly of β-amyloid peptide. *Biophys. J. 69*, 640–651.
65. Jansen, R..; et al. (2004) High Pressure Promotes Circularly Shaped Insulin Amyloid. *J. Mol. Biol. 338*, 203–206.
66. Sciarretta, K..; et al. (2005) Aβ40-Lactam(D23/K28) Models a Conformation Highly Favorable for Nucleation of Amyloid. *Biochemistry 44*, 6003–6014.
67. Yankner, B., Duffy, L., and Kirschner, D. (1990) Neurotrophic and neurotoxic effects of amyloid β protein: Reversal by tachykinin neuropeptides. *Science 250*, 279–282.
68. Roher, A..; et al. (1991) β-Amyloid from Alzheimer disease brains inhibits sprouting and survival of sympathetic neurons. *Biochem. Biophys. Res. Commun. 174*, 572–579.
69. Kayed, R..; et al. (2003) Common Structure of Soluble Amyloid Oligomers Implies Common Mechanism of Pathogenesis. *Science 300* (5618), 486–488.
70. Lorenzo, A., and Yankner, B. (1994) β-Amyloid neurotoxicity requires fibril formation and is inhibited by congo red. *Proc. Natl. Acad. Sci. U.S.A. 91* (25), 12243–12247.
71. Cranford, S. W., and Buehler, M. J. (2009) Mechanomutable carbon nanotube arrays. *Int. J. Mater. Struct. Integr. 3* (18), 161–178.